Part-to-Itself Model Inversion in Process Compensated Resonance Testing

Alexander Mayes[2,a)], Leanne Jauriqui[2,b)], Eric Biedermann[2,c)], Julieanne Heffernan[2,d)], Richard Livings[2,e)], John C. Aldrin[3,f)], Brent Goodlet[4,g)], Siamack Mazdiyasni[1,h)]

[1]*Air Force Research Laboratory (AFRL/RXCA), Wright-Patterson AFB, OH, USA*
[2]*Vibrant Corporation, Albuquerque, NM, USA*
[3] *Computational Tools, Gurnee, IL, USA*
[4]*University of California, Santa Barbara, Santa Barbara, CA, USA*

[a)] Corresponding author: amayes@vibrantndt.com
[b)] ljauriqui@vibrantndt.com
[c)] ebiedermann@vibrantndt.com
[d)] jheffernan@vibrantndt.com
[e)] rlivings@vibrantndt.com
[f)] aldrin@computationaltools.com
[g)] bgoodlet@engineering.ucsb.edu
[h)] siamack.mazdiyasni@us.af.mil

Abstract. Process Compensated Resonance Testing (PCRT) is a non-destructive evaluation (NDE) method involving the collection and analysis of a part's resonance spectrum to characterize its material or damage state. Prior work used the finite element method (FEM) to develop forward modeling and model inversion techniques. In many cases, the inversion problem can become confounded by multiple parameters having similar effects on a part's resonance frequencies. To reduce the influence of confounding parameters and isolate the change in a part (e.g. creep), a part-to-itself (PTI) approach can be taken. A PTI approach involves inverting only the change in resonance frequencies from the before and after states of a part. This approach reduces the possible inversion parameters to only those which change in response to in-service loads and damage mechanisms. To evaluate the effectiveness of using a PTI inversion approach, creep strain and material properties were estimated in virtual and real samples using FEM inversion. Virtual and real dog bone samples composed of nickel-based superalloy Mar-M-247 were examined. Virtual samples were modeled with typically observed variations in material properties and dimensions. Creep modeling was verified with the collected resonance spectra from an incrementally crept physical sample. All samples were inverted against a model space that allowed for change in the creep damage state and the material properties but was blind to initial part dimensions. Results quantified the capabilities of PTI inversion in evaluating creep strain and material properties, as well as its sensitivity to confounding initial dimensions.

INTRODUCTION

Process Compensated Resonance Testing (PCRT) is a non-destructive evaluation (NDE) method involving the collection and analysis of a part's resonance spectrum to evaluate its material or damage state [1]. Historically, applications of PCRT have evaluated parts on a pass or fail basis, determining if a part is good or bad by training pattern recognition algorithms to the spectra of known good and bad populations, and then sorting the part based on its similarity to both populations [2]. While this approach is often sufficient from a quality control standpoint, it is often desirable to more fully characterize a defective part to better understand the nature and root cause of the defect/damage. To this end, recent PCRT research has focused on developing modeling capabilities to investigate

how and which resonance modes of a given part will react to changes in material, geometry, or even damage state [3-4]. Using the finite element method (FEM), a part's resonance frequencies can readily be produced from a given set of defining parameters.

The inverse problem, determining a part's defining parameters from its resonance frequencies, is often not as straightforward. Model inversion using resonant ultrasound spectroscopy (RUS) is an established solution to this problem but has largely been limited to characterizing bulk elastic properties in simple coupon geometries [5-6]. Recent work in developing RUS has addressed samples of arbitrary geometry [7,8], multiple misaligned crystals [9,10], defects and damage states [4,11], and the use of FEM to enhance RUS capabilities [3,12]. By introducing FEM forward modeling, the inversion problem can be expanded to cover complex geometries, materials, and damage states. However, in doing so, the complexity of the problem increases; extra dimensions, localized material properties, and damage states such as cracking and creep can quickly increase the dimensionality of an inversion problem. This increase in dimensionality not only has a steep computational cost, but can also cause the problem to become ill-posed.

In cases where the parameters of interest are the changes between two states of a part, such as evaluating a part before and after a service cycle to characterize potential damage, a part-to-itself (PTI) approach can alleviate many of these issues. PTI involves analyzing the changes in a part's resonance frequencies between states, rather than the absolute frequencies themselves. By doing so, the resonance effects of many of the aforementioned confounding factors that do not change between states will be minimized, homing in on only those parameters that are changing. The PTI approach has previously been implemented in PCRT sorting solutions. This study examines the application of a PTI approach to the model inversion problem by attempting to quantify creep strain in nickel-based superalloy dog bone coupons and comparing the results to a non-PTI inversion method.

INVERSION METHODS

PCRT Model Inversion

Model inversion, in the context of PCRT, refers to the estimation of a set of parameters that describe a sample using its resonance frequencies. This is done by iteratively modeling frequencies from different combinations of parameters until there is a satisfactory match between the modeled frequencies and the sample frequencies. Figure 1 shows this process in more detail.
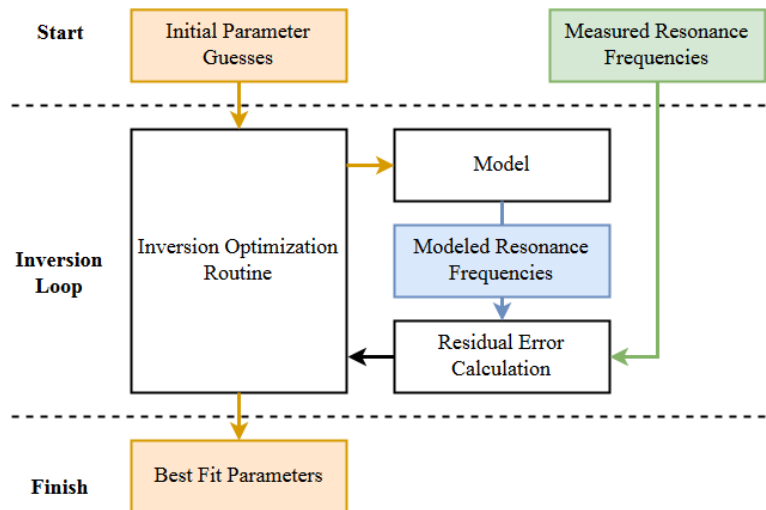
FIGURE 1. Diagram of general PCRT model inversion

To begin, the measured resonance frequencies of the sample are passed to the inversion code, along with some initial guesses as to what the parameter values might be. These initial parameters can be educated guesses based on literature or random guesses within the problem bounds. They are then passed to the inversion model, which calculates what the resonance frequencies would be for that set of parameters. The modeled frequencies are then

compared to the measured sample frequencies and the sum-of-squares of the residual errors (SSE) is passed to the optimization routine. The optimization routine makes changes to the parameter values based on the SSE. The process is repeated until a convergence criterion has been met: either the SSE is below a certain threshold or is not changing appreciably with further iterations. For this study, a non-linear least squares approach was taken for optimization using a trust-region-reflective algorithm [13]. Because non-linear least squares estimation is not guaranteed to find a global solution, multiple repetitions of each inversion were performed using different initial values. Initial values were chosen pseudo-randomly using Latin hypercube sampling to ensure that the full range of parameter values in the given bounds was represented [14]. The best fit solution was then chosen as whichever repetition had the lowest SSE.

The inversion model that has historically been used in resonance inversion is an energy minimization technique that finds resonances of a solid body by approximating solutions of the mechanical Lagrangian [5-6]. While this approach is computationally inexpensive, it is limited to simple, elastically homogenous geometries such as spheres, rectangular parallelepipeds, and cylinders. To perform inversion of more complex geometries and material characteristics, and damage states, an FEM modeling approach was implemented. Because FEM has a relatively high computational cost per model, and the inversion model must be called at every iteration, a surrogate model was created to serve as the actual inversion model. This surrogate model quickly interpolates over a pre-generated grid of FEM model solutions [15]. While this approach introduces some additional uncertainty in the form of surrogate model interpolation error, it allows for fast inversion while still taking advantage of FEM's ability to model complex parts.

Part-to-Itself Inversion

Two approaches to PTI inversion were evaluated in this study and will hereon be referred to as Method 1 and Method 2. Each method has inherent advantages and disadvantages, which will be discussed below. Figure 2 shows a diagram of Method 1, illustrating that it shares an identical algorithm to general inversion, but with parameters and frequencies replaced with *parameter changes* and *resonance changes*. This similarity makes the implementation of this method fairly straightforward, allowing for code that can easily perform both general and PTI inversion. Additionally, the inversion model is, at least partly, composed of changes between FEM models. This usually requires some assumptions during setup of the inversion model space as to absolute parameter values and which parameters will change. In cases like crystal orientation, relative changes cannot be generalized because they are so dependent on the absolute orientation (e.g. 10°-15° $\neq$ 45°-50°), and modeling every combination would increase the dimensionality of the problem. In such a case, it is often more practical to make educated assumptions about how a parameter might change (or not change).
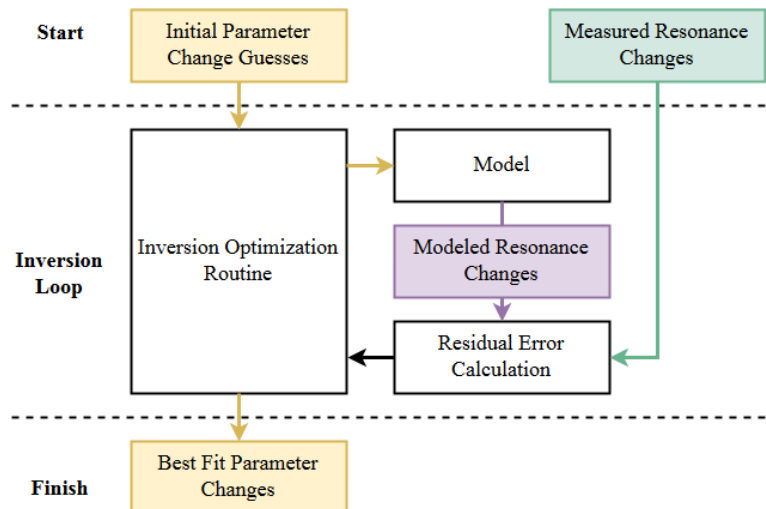
FIGURE 2. Diagram of part-to-itself inversion Method 1

The diagram of Method 2, shown in Fig. 3, illustrates a similar design to Method 1 with a slight increase in complexity; instead of using changes for both frequencies and parameters, changes in frequencies are used with

absolute parameters for the initial and final states. The inversion model in this case is constructed the same way it would be in non-PTI inversion and returns absolute frequencies given absolute parameters for both states. The modeled frequency changes are then calculated by taking the difference. This approach alleviates the need to make assumptions about parameter values and which parameters will change, but effectively doubles the number of parameters of the inversion problem, increasing the difficulty for the optimization routine.
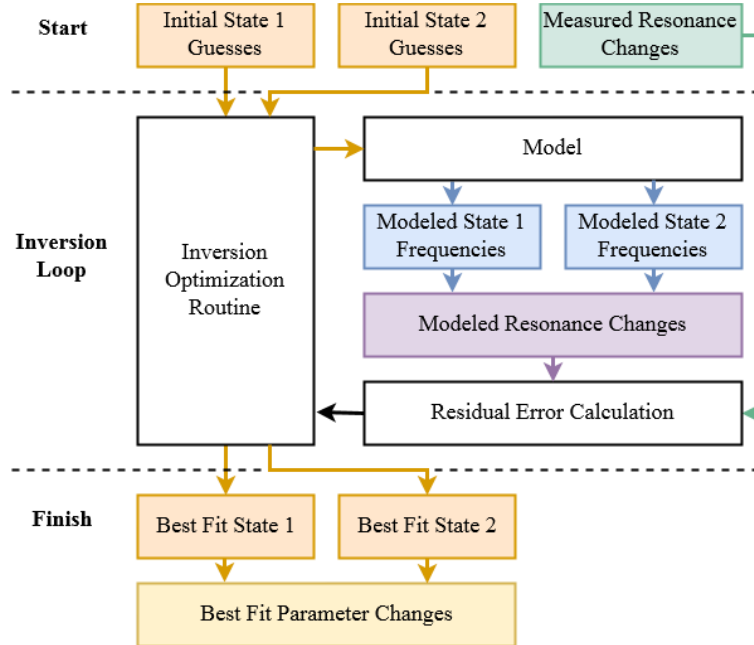
FIGURE 3. Diagram of part-to-itself inversion Method 2

SOURCES OF UNCERTAINTY

In the evaluation of inversion methods, several sources of uncertainty must be considered and addressed. These sources can generally be broken down into two categories: aleatory and epistemic uncertainty. Aleatory uncertainty encompasses the inherent randomness in a system. In the case of PCRT inversion it refers to part-to-part variation, such as random material property, crystal orientation, and dimensional variation, as well as shot-to-shot measurement variation in the collection of resonance spectra. Work done by Biedermann et al. [16] addressed the relative impact of these aleatory sources and found part-to-part variation was the dominant driver of uncertainty while shot-to-shot measurement variation was a small contributor. Based on these findings, this study focused on addressing part-to-part variation and used an average of shot-to-shot measurements. Epistemic uncertainty encompasses system parameters that are assumed to have a fixed but unknown value. This includes (but is not limited to) mesh uncertainty, inherent in discretizing a part into finite elements, the aforementioned surrogate model uncertainty due to interpolation error, and the presence of un-modeled or oversimplified parameters. Part-to-itself inversion will ideally mitigate the latter source by eliminating the effects of those un-modeled or oversimplified parameters that do not change between states. Epistemic uncertainty also includes uncertainty in the convergence of the optimization routine due to false local minima. Simultaneous work devoted to quantifying the uncertainty of the methods described here will be presented in [15] and thus will not be discussed in this paper.

MODEL SETUP

The part used in this study was an axisymmetric dog bone coupon geometry, shown in Fig. 4, composed of single crystal Mar-M-247. Mar-M-247 is a nickel-based superalloy with cubic symmetry and thus has three degrees of freedom in material properties, defined here as Young's modulus (E_{001}), Poisson's ratio (ν), and Zener anisotropy ratio (A). For a single crystal specimen, crystal orientation must also be defined and, due to the axisymmetry of the part, may be approximated by a single crystal angle (θ): that between the axis of symmetry of the part (Z axis in Fig.

4) and the [001] crystallographic vector. Additionally, Fig. 4 denotes the initial (undeformed) part dimensions that were shown to have a more substantial effect on resonance [17]: gauge diameter (D_{gauge}), gauge length (L_{gauge}), and grip lengths (L_{grip}). The final model parameter considered is creep strain, which was chosen as the damage mode of interest for this study. Prior work by Goodlet et al. [11] identified shape deformation as the dominant factor in resonance changes due to creep and established a reliable method for modeling these changes. Constraints and loads were applied as they would be in an experimental creep setup, shown in Fig. 5, and the Hill yield criterion used to simulate anisotropic flow [18].
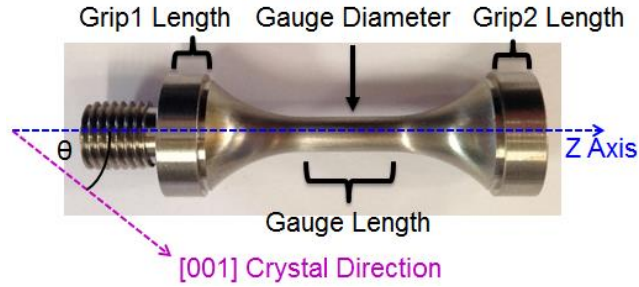
FIGURE 4. Dog bone coupon geometry with dimension and crystal orientation parameter labels
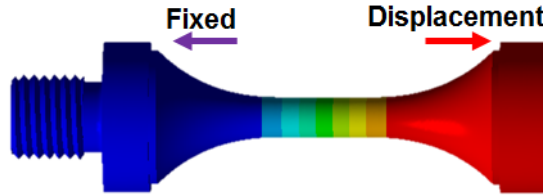
FIGURE 5. Dog bone model showing creep constraint and applied load

TABLE 1. Parameter values for the bounds of the inversion space, the nominal part, and the modeled inversion inputs. Note that creep is given as a percent of the nominal gauge length (10 mm)

Parameter	Inversion Model Space				Modeled Input Points			
	Range	Min	Nominal	Max	Mod-1	Mod-2	Mod-3	Mod-4
E_{001} (GPa)	+/- 2.00%	125.18	127.73	130.29	125.76	128.91	127.61	130.14
ν_{001}	+/- 7.00%	0.35	0.37	0.40	0.36	0.36	0.38	0.39
A	+/- 5.00%	2.62	2.75	2.89	2.84	2.82	2.64	2.69
θ (°)	0-10.00	0.00	0.00	10.00	0.72	6.80	8.57	2.64
D_{gauge} (mm)	N/A	N/A	4.00	N/A	4.02	3.98	3.99	4.01
L_{gauge} (mm)	N/A	N/A	10.00	N/A	9.93	9.98	10.08	10.02
L_{grip1} (mm)	N/A	N/A	4.50	N/A	4.52	4.53	4.46	4.48
L_{grip2} (mm)	N/A	N/A	4.50	N/A	4.54	4.48	4.51	4.47
Creep (%)	0-12.00	0.00	0.00	12.00	3.90	1.30	4.60	6.10

To address the more prominent sources of aleatory uncertainty discussed earlier, the modeled inversion space explored variation in all of the material and crystal orientation parameters in established ranges for the acquired specimens [16]. Creep strain was also included in the inversion space as the primary parameter of interest. To compare the inversion methods with known parameters, four modeled input points were generated with random variation in all of the parameters included in the inversion space, as well as variation in the initial dimensions to evaluate the methods' performance in the presence of un-modeled parameters, addressing epistemic uncertainty. Table 1 provides bounds for the inversion space, the nominal model parameter values, and the parameter values for the modeled inversion input.

RESULTS AND DISCUSSION

Modeled Inversion Results

Figures 6-7 plot the inversion results for the modeled input points; Fig. 6 shows the best fit creep value for each method plotted against the known input value and Fig. 7 plots the absolute error of those results in percent strain. Overall, inversion using the PTI methods proved to be consistently as good as or better than using the general approach with error for both methods falling within 0.25% strain for every sample. Between the PTI methods, Method 1 was slightly more accurate than Method 2. A possible explanation for this lies in the assumptions made in creating the surrogate model for Method 1. In order to keep the surrogate model to a reasonable size, it was necessary to assume that crystal orientation (θ) would remain constant between the different creep increments due to its complex interaction with other parameters. This assumption was inherently true for the modeled input due to the methods used for modeling creep. Method 2 did not require this assumption and thus may have converged to local minima with some crystal orientation angle change between states.

Table 2 provides inversion results for the material parameters. Because the only change between initial and final states for the modeled inputs was elongation due to creep, all of these parameters should ideally converge to zero; thus this table can also serve as a summary of inversion error. It confirms that the best fit results for Method 2 did indeed converge to non-zero crystal orientation change, though very small θ in most cases. Examination of the remaining parameters reveals that no method is consistently more accurate for estimation of v_{001} or A, though PTI inversion performed slightly better for E_{001}.
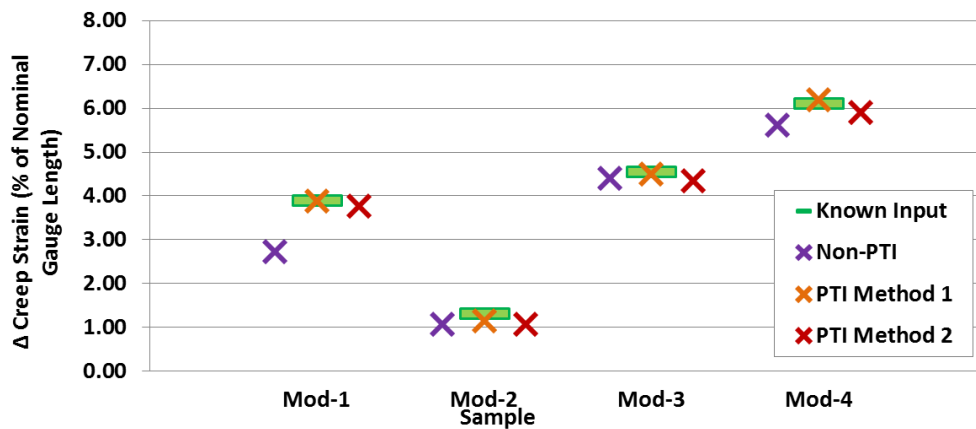
FIGURE 6. Inversion estimates of creep strain for modeled input
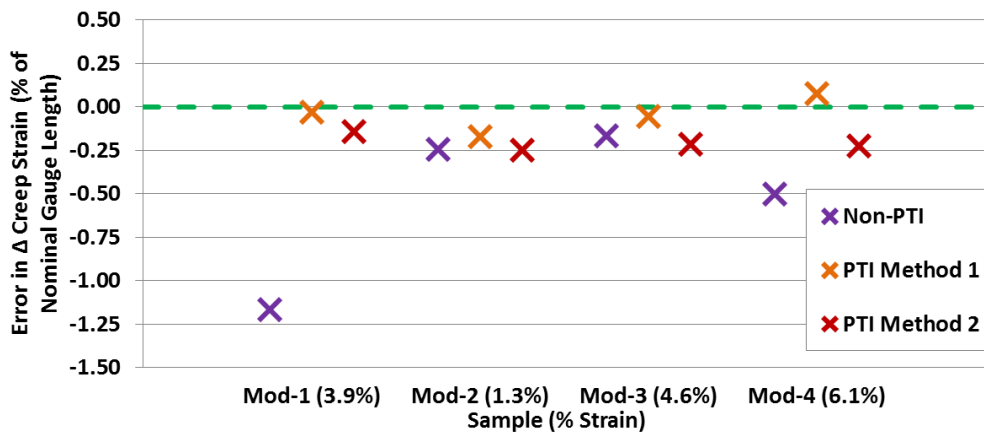
FIGURE 7. Error in inversion estimates of creep strain for modeled input

TABLE 2. Modeled input inversion results for change in material properties and crystal orientation

	Sample	Mod-1	Mod-2	Mod-3	Mod-4
	Non-PTI	-0.37	-0.04	-0.03	-0.12
ΔE_{001} (%)	Method 1	0.00	-0.02	0.02	0.04
	Method 2	-0.02	-0.04	-0.03	0.02
	Non-PTI	-1.60	-0.41	-0.24	-0.48
Δv_{001} (%)	Method 1	-0.09	-0.18	0.36	0.18
	Method 2	-0.25	-0.37	-0.27	0.03
	Non-PTI	-0.50	-0.11	-0.08	-0.36
ΔA (%)	Method 1	-0.01	-0.10	-0.14	-0.02
	Method 2	-0.07	-0.14	-0.11	-0.17
	Non-PTI	-2.20	0.03	0.03	-0.75
$\Delta\theta$ (°)	Method 1	N/A	N/A	N/A	N/A
	Method 2	0.07	0.02	0.01	-0.60

Experimental Verification

To verify the advantages of PTI experimentally, a physical coupon of the modeled geometry was incrementally crept, and resonance data was collected after each subsequent change in length. Using the same experimental setup described in [11], the sample was heated to 950° C with a 300 MPa load in an open-air clam-shell furnace. Table 3 provides strain and test time data for each creep increment. Although resonance spectra were collected at every increment, inversion was only performed for the first four increments; creep above 10% strain was deemed not of interest primarily due to its ease of detection by simple visual inspection as well as the necessity to detect creep defects prior to reaching critical stages.

TABLE 3. Experimental creep increments with corresponding strains and test times

Increment	Dog Bone Strain (% of Nominal Gauge Length)	Test Time (h)
Exp-1	0.2	0.4
Exp-2	0.6	1.2
Exp-3	3.2	13.5
Exp-4	9.1	26
Exp-5	10.1	27
Exp-6	11	28
Exp-7	12.3	29
Exp-8	14	30
Exp-9	17	32

Figure 8 presents a comparison of frequency shifts for modeled versus measured creep for 3.2% creep strain. There is good agreement between the measured and modeled frequency shifts, particularly in the pattern of which modes are more or less affected by creep. Because the inversion algorithm optimizes to the SSE it is particularly sensitive to the patterns of frequency change and likely to home in on the correct solution. However, there is also a slight, but consistent, overestimation in frequency change by the model. This is because of the overall upward shift in measured frequencies in the first creep increment, which is consistent with the findings in [11] but not accounted for in the creep model. The cause of this shift is still uncertain.
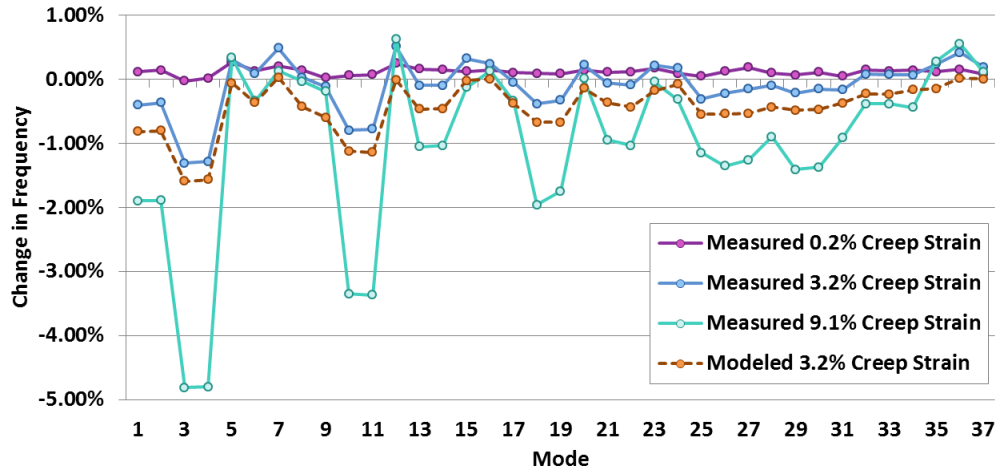
FIGURE 8. Frequency changes by mode due to modeled and measured creep

Figures 9-10 plot the inversion results for the first four increments of the experimentally crept sample. While all three inversion methods still performed well, the accuracy distinction between the PTI methods and the general approach that was present in the modeled input inversion was no longer apparent for the measured. Non-PTI accuracy floated between $\pm$ 0.25% strain for all levels of creep. The PTI methods did show improved accuracy at the lower creep levels, which is encouraging as earlier detection is always preferable. This trend may be due to simplifications in the creep modeling breaking down at higher levels of creep or uncertainty in the creep measurements of the sample. Additionally, the lower levels of creep showed nearly identical results between Method 1 and Method 2, possibly indicating that the assumptions of unchanging crystal orientation in Method 1 were invalid or that the additional uncertainties introduced in using measured inputs (such as noise or inhomogeneities in the part) reduced the possible local minima. Although additional tests were not performed to verify the inversion accuracy of the remaining inversion parameters (E, ν, A, θ), valuable conclusions can still be drawn from the best-fit results, presented in Table 4. Unlike the current creep model, which does not account for change in material parameters, E_{001} exhibited a steady increase with increasing creep increments while A exhibited a steady decrease. The changes in these parameters may indicate areas for further investigation in creep modeling techniques. Additionally, though most of the best fit changes were fairly consistent between the three methods for the first three creep increments, the same cannot be said for Exp-4. This break in trend lends credence to the theory that the creep model loses accuracy at higher levels of strain, and the non-geometric effects of creep begin to play a more important role in resonance.
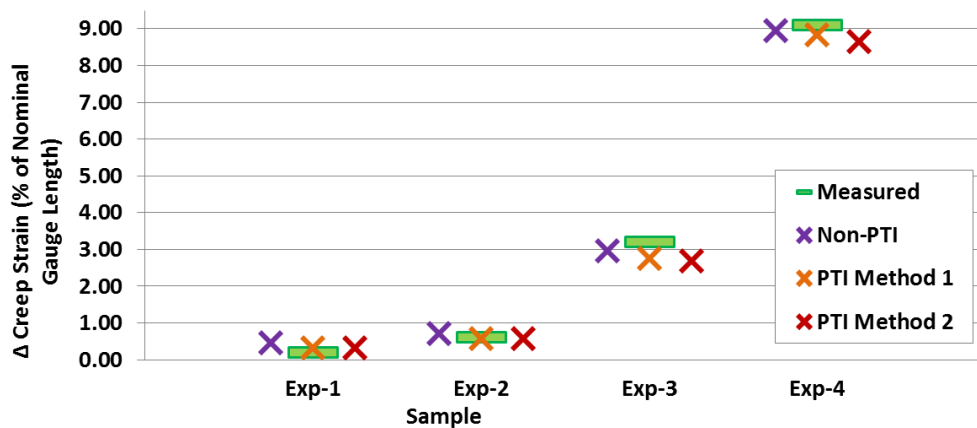
FIGURE 9. Inversion estimates of creep strain for measured input
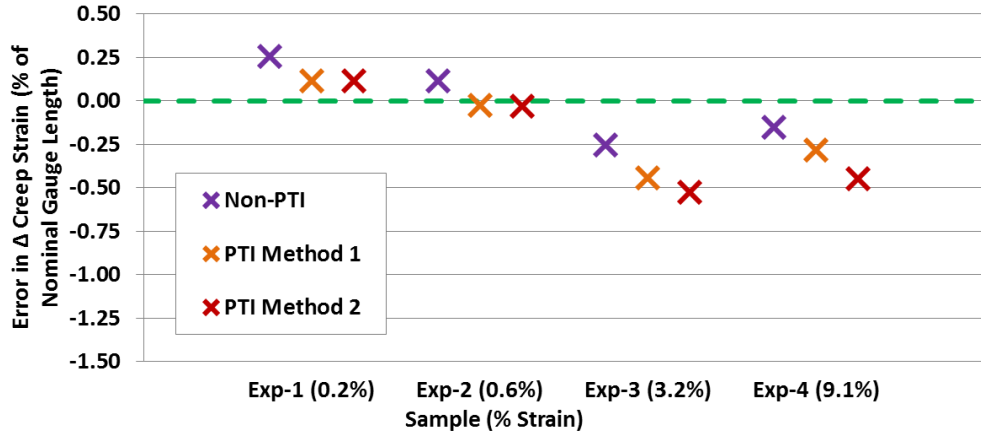
FIGURE 10. Error in inversion estimates of creep strain for measured input

TABLE 4. Measured input inversion results for change in material properties and crystal orientation

	Sample	Exp-1	Exp-2	Exp-3	Exp-4
ΔE_{001} (%)	Non-PTI	0.37	0.56	0.84	1.13
	Method 1	0.37	0.56	0.82	0.91
	Method 2	0.38	0.58	0.86	0.99
Δv_{001} (%)	Non-PTI	0.13	0.06	0.03	0.39
	Method 1	0.14	0.08	-0.12	1.30
	Method 2	0.10	0.06	-0.31	-0.15
ΔA (%)	Non-PTI	-0.05	-0.16	-0.36	-0.69
	Method 1	-0.06	-0.16	-0.38	0.21
	Method 2	-0.11	-0.23	-0.50	-0.57
$\Delta \theta$ (°)	Non-PTI	0.08	0.10	0.00	-0.65
	Method 1	N/A	N/A	N/A	N/A
	Method 2	0.06	0.03	0.03	-2.26

CONCLUSION

PTI inversion mitigates the effects of confounding parameters and aleatory uncertainty sources and has the potential to provide better parameter estimates than non-PTI inversion of RUS data. Two part-to-itself inversion methods were developed to extract information about changes in the part's material and damage state. Method 1 uses the established structure of general resonance inversion by simply replacing frequency and input parameter values with changes in those values. Method 2 generates parameters and frequencies for the initial and final part states and optimizes those parameters using solely the change in frequencies. Results demonstrate that both PTI methods have consistently superior inversion accuracy over non-PTI inversion when using modeled sample inputs. Method 1 slightly out-performed Method 2 in all cases. Experimental verification was performed by iteratively creeping a dog bone specimen and collecting spectra at multiple strain levels. Inversion results using these spectra as inputs found that the PTI methods' improved accuracy held at lower levels of creep, generally considered to be more critical for early detection, but less so at higher levels. Future work will continue to investigate both PTI methods, as well as a combined PTI and absolute approach, using a more robust sample population (virtual and experimental) and more complex geometries, such as an airfoil.

ACKNOWLEDGEMENTS

REFERENCES

1. ASTM Standard E2534-15, 2015, "Standard Practice for Process Compensated Resonance Testing via Swept Sine Input for Metallic and Non-Metallic Parts, ASTM International, www.astm.org.
2. J. Schwarz, J. Saxton, and L. Jauriqui, "Process Compensated Resonant Testing in Manufacturing Process Control," *Material Evaluation*, **63**, pp. 736-739, (2005).
3. E. Biedermann, L. Jauriqui, J. C. Aldrin, B. Goodlet, T. Pollock, C. Torbet, and S. Mazdiyasni, "Resonance ultrasound spectroscopy forward modeling and inverse characterization of nickel-based superalloys," *41st Annual Review of Progress in QNDE, AIP Conf. Proc*, **1650**, pp. 835-844, (2015).
4. J. Heffernan, L. Jauriqui, E. Biedermann, A. Mayes, R. Livings, B. Goodlet, and S. Mazdiyasni, "Process compensated resonance testing models for quantification of creep damage in single crystal nickel-based superalloys" *Materials Evaluation*, **75**, n 7, pp. 941-952, (2017).
5. A. Migliori, J. Sarrao, M. W. Visscher, T. Bell, M Lei, Z. Fisk, and R. Leisure, ''Resonant ultrasound spectroscopy techniques for measurement of the elastic moduli of solids,'' *Physica B*, **183**, pp. 1–24, (1993).
6. A. Migliori, and J. L. Sarrao, *Resonant Ultrasound Spectroscopy*, New York, Wiley, (1997).
7. G. Liu, and J. D. Maynard, "Measuring elastic constants of arbitrarily shaped samples using resonant ultrasound spectroscopy," *Journal of the Acoustical Society of America*, **131**, n. 3, pp. 2068-2078, (2012).
8. M. C. Remmillieux, T. J. Ulrich, C. Payan, J. Riviere, C. R. Lake, and P.-Y. Le Bas, "Resonant ultrasound spectroscopy for materials with high damping and samples with arbitrary geometry," *Journal of Geophysical Research: Solid Earth*, **120**, pp. 4898-4916, (2015).
9. L. H. Rettberg, B. R. Goodlet, T. M. Pollock, "Detecting recrystallization in a single crystal Ni-base alloy using resonant ultrasound spectroscopy," *NDT & E International*, **83**, pp. 68-77, (2016).
10. T. J. Lesthaeghe, R. A. Adebisi, S. Sathish, M. R. Cherry, and P. A. Shade, "Toward characterization of single crystal elastic properties in polycrystalline materials using resonant ultrasound spectroscopy," *Materials Evaluation*, **75**, n 7, pp. 930-940, (2017).
11. B. R. Goodlet, C. J. Torbet, E. Biedermann, L. Jauriqui, J. C. Aldrin, and T. M. Pollock, "Forward models for extending the mechanical damage evaluation capability of resonant ultrasound spectroscopy," *Ultrasonics*, **77**, pp. 183-196, (2017).
12. J. Plesek, R. Kolman, and M. Landa, "Using finite element method for the determination of elastic moduli by resonant ultrasound spectroscopy," *Journal of the Acoustical Society of America*, **116**, n. 1, pp. 282-287, (2004).
13. Web site: https://www.mathworks.com/help/optim/ug/choosing-the-algorithm.html#bsbwx11
14. R. L. Iman, J. M. Davenport, D. K. Zeigler, *Latin Hypercube Sampling (Program User's Guide)*, Albuquerque, Sandia Laboratories and Texas Tech University, (1980).
15. J. C. Aldrin, A. Mayes, L. Jauriqui, E. Biedermann, J. Heffernan, R. Livings, B. Goodlet, S. Mazdiyasni, "Uncertainty Quantification of Resonant Ultrasound Spectroscopy for Material Property and Single Crystal Orientation Estimation on a Complex Part," *44th Annual Review of Progress in QNDE*, AIP Conf. Proc., (expected, 2018).
16. E. Biedermann, L. Jauriqui, J. C. Aldrin, A. Mayes, T. Williams, and S. Mazdiyasni, "Uncertainty quantification in modeling and measuring components with resonant ultrasound spectroscopy," *42nd Annual Review of Progress in QNDE, AIP Conf. Proc*, **1706**, p. 070008, AIP Publishing, (2016).
17. E. Biedermann, J. Heffernan, A. Mayes, G. Gatewood, L. Jauriqui, B. Goodlet, S. Mazdiyasni, "Process compensated resonance testing modeling for damage evolution and uncertainty quantification," *43rd Annual Review of Progress in QNDE*, AIP Conf. Proc, **1806**, p. 090005, (2017).
18. A. D. Ramaglia and P. Villari, "Creep and Fatigue of Single Crystal and Directionally Solidified Nickel-base Blades via a Unified Approach Based on Hill48 Potential Function: Part 1 Plasticity and Creep," *Proceedings of ASME Turbo Expo 2013: Turbine Technical Conference and Exposition*. GT2013-94675. (2013).